symmetry

MDPI

Article

Time-Varying Ultra-Wideband Channel Modeling and Prediction

Ahmed M. Al-Sammna *, Marwan Hadri Azmi and Tharek Abd Rahman

Wireless Communication Centre, Faculty of Engineering, Universiti Teknologi Malaysia, Johor Bahru 81310, Malaysia; hadri@fke.utm.my (M.H.A.); tharek@fke.utm.my (T.A.R.)

* Correspondence: ahmedsecure99@gmail.com; Tel.: +60-11-116-23478

Received: 9 October 2018; Accepted: 20 October 2018; Published: 12 November 2018

Abstract: This paper considers the channel modeling and prediction for ultra-wideband (UWB) channels. The sparse property of UWB channels is exploited, and an efficient prediction framework is developed by introducing two simplified UWB channel impulse response (CIR) models, namely, the windowing-based on window delay (WB-WD) and the windowing-based on bin delay (WB-BD). By adopting our proposed UWB windowing-based CIR models, the recursive least square (RLS) algorithm is used to predict the channel coefficients. By using real CIR coefficients generated from measurement campaign data conducted in outdoor environments, the modeling and prediction performance results and the statistical properties of the root mean square (RMS) delay spread values are presented. Our proposed framework improves the prediction performances with lower computational complexity compared with the performance of the recommended ITU-R UWB-CIR model. It is shown that our proposed framework can achieved 15% lower prediction error with a complexity reduction by a factor of 12.

Keywords: channel impulse response; channel prediction; recursive least square; ultra-wideband channel propagation measurement

1. Introduction

The Federal Communications Commission (FCC) defines ultra-wideband (UWB) communications [1,2] as systems that operate within the fractional bandwidth of $B/f_c \geq 20\%$, where B is the transmission bandwidth and f_c is the center frequency of the band, or with a total bandwidth of more than 500 MHz [3,4]. The UWB systems are currently deployed on an unlicensed frequency band of 3.1 GHz to 10.6 GHz [5]. However, under the FCC definition, practical UWB communication systems may include some existing systems, such as long-term evolution (LTE) and LTE advanced (LTE-A) utilizing the single carrier (SC) frequency division multiplexing access (FDMA) scheme [6–9], 60 GHz WLAN [10,11] and future 5G wireless communications [12–14] operating at millimetre wave (mm-wave). According to the Mobile and Wireless Communication Enablers for the Twenty-Twenty Information Society (METIS 2020) project, the bandwidth for 5G systems ranges from 0.5 GHz to 2 GHz and operates within the candidate frequency band range of 0.45 GHz to 85 GHz [15]. The key to harvesting this high bandwidth advantage of UWB wireless communication systems is understanding their channels' characteristics and behaviors. Many works have been dedicated to studying the propagation channels of large bandwidth systems in different environments [16–24]. In [16], the path loss and multipath parameters were investigated based on propagation measurement using UWB signals in a forest environment. Based on the measurements conducted in an indoor environment, the work of [17] modified the CLEAN algorithm to estimate the time-of-arrival, angle-of-arrival, and waveform shape. In [18], the fundamental differences between UWB and other wireless channels, e.g., narrowband and wideband, were discussed. A three-dimensional (3D)

ray-tracing model that can support a detailed representation of an indoor environment and the external building structures was developed in [19]. Extensive measurements were conducted to characterize and model UWB channels for the future 5G large bandwidth systems in different indoor [20–22] and outdoor environments [23,24]. In addition, a better understanding of UWB propagation channels helps in the investigation of the communication-theoretic and information-theoretic limits for an optimum UWB system, including 5G technology designs [25,26]. Adaptive transmission methods with accurate channel state information (CSI) have shown great potential in achieving high rates of data transmission [13,27,28]. The CSI is estimated at the receiver and then fed back to the transmitter to improve the upcoming transmission. Channel estimation works well for time-invariant channels where the statistics of the channel are strict-sense stationary. For time-variant channels, the estimated CSI fed from the receiver to the transmitter may already be outdated because of the computational and propagation delays. It has been shown that using this estimated and outdated CSI for adaptive transmission systems with fast channel variation degrades performances [27]. An alternative approach to overcome this problem is to predict the CSI ahead of time and to use it in the upcoming transmission. For narrowband (NB) systems, the Wiener filtering is used to compute the predictor coefficients in [29]. Here, the two-step channel-prediction technique is proposed for use in the orthogonal frequency-division multiplexing (OFDM) and frequency division duplex (FDD) systems supporting adaptive modulation and coding (AMC) schemes over time-varying multipath fading channels. The work of [30] involved a comparative study between two time-domain prediction strategies, namely, the adaptive minimum mean square error (MMSE) and the recursive least square error (RLS) predictors, in time-varying wireless channels.

A probabilistic channel prediction framework that predicts the spatial variations of wireless channels using a small number of measured data was developed in [31]. This proposed framework was then tested using real channel measurements covering different indoor environments. In [32], the performance of an autoregressive (AR) model-based linear predictor in moderate and fast fading channels was studied. In NB channels, all multipath components (MPCs) fall into one single resolvable delay bin because the maximum access delay is smaller than the inverse bandwidth [18]. As the bandwidth increases in wideband (WB) channels, several delay bins arise where each bin contains multiple MPCs, leading to fading in each separate bin [18]. Because of the fine time resolution from having very large bandwidths for UWB channels, each delay bin contains only one or no MPCs at all [33]. As a result, the bins containing a single MPC are interspersed with empty bins, resulting in a sparse channel impulse response (CIR) for UWB systems [14]. This sparse CIR property was found in future 5G wireless systems operating at mm-wave spectrum bands [14].

For time-varying UWB channels resulting from the movement of the transmitter, receiver, and/or scatterers, the MPCs move from one delay bin to another on a very fast time scale in the order of tens of milliseconds [34,35]. This movement causes the stochastic process of the channel taps in UWB-CIR to be dependent across delay and consequently, makes it a challenge to predict the next CIR. The work of [34], however, illustrated that the UWB-CIR prediction is still viable by tracking the time evolution of each MPC separately across the delay variable. Here, because of the large number of MPCs in UWB-CIR, tracking each MPC for prediction increases the signal processing complexity of the communication systems; such increased complexity is incompatible for 5G mission-critical services with a very low-latency requirement. This work addresses these complexity issues of UWB-CIR prediction.

The contributions of this work are threefold. First, we generalize the concept of the windowing-based CIR model by proposing two less-complex UWB-CIR models for channel predictions, namely, the windowing-based on window delay (WB-WD) model and the windowing-based on bin delay (WB-BD) model. The windowing-based models are different from the Saleh–Valenzuela (SV) model [36] in the sense that the grouping of the CIR taps is based on an equal and structured window size that acts as a tool to simplify channel prediction, whereas the SV model is based on the assumption that MPCs arrive in clusters. As a result, the proposed windowing-based models can be used to simplify any CIR, including the CIR from the cluster-based models, such that a less-complex channel

prediction can be achieved. Second, based on our proposed models, the UWB-CIR prediction using the RLS algorithm is analyzed. The complexity reduction analysis when adopting this model is also presented. Third, the modeling and prediction performance results and the statistical properties of the root mean square (RMS) delay spread are presented. These results are generated by utilizing the proposed windowing-based models on the measured UWB-CIRs from an outdoor measurement campaign. The remainder of this paper is organized as follows. In Section 2, the UWB channel impulse response is presented. The two proposed window-based UWB-CIR models are developed in Section 3. The CIR tap prediction using the RLS algorithm for the proposed window-based CIR is presented in Section 4. Section 5 presents the performance evaluation, and Section 6 provides the computation complexity analysis. The modeling and prediction performance results are presented in Section 7. Finally, the paper is concluded in Section 8.

2. UWB Channel Impulse Response

2.1. Channel Model

The static multipath UWB channels, assuming no pulse distortion for simplicity, can be represented using an L-tapped delay line model:

$$h(\tau) = \sum_{i=0}^{L-1} \alpha_i \delta(\tau - m_i), \tag{1}$$

where $\delta(\cdot)$ corresponds to a Dirac delta function, and the coefficients α_i and m_i are the i-th tap gain and delay, respectively. For time-varying channels, (1) can be modeled as

$$h(t, \tau) = \sum_{i=0}^{L-1} \alpha_i(t) \delta(\tau - m_i(t)), \tag{2}$$

where t is either the time or the spatial location. Assuming that the transmitter moves at a constant velocity away from the receiver, the conversion between the time and spatial location parameters is straightforward [34]. Hence, the two parameters are used interchangeably in this work. For real communication systems, the space and delay must be sampled. Using T_s to denote the sampling period over delay and Δd to denote the sampling distance between the Rx and Tx antennas, the discrete form of (2) when applying the transformations of $\tau = mT_s$ and $t = p\Delta d$ is

$$h(p\Delta d, mT_s) = \sum_{i=0}^{L-1} \alpha_i(p\Delta d) \delta(mT_s - m_i(p\Delta d)), \tag{3}$$

where $m \in \{1, \ldots, N\}$ is the delay index and $p \in [1, \ldots, P]$ is the position or location index for Tx or Rx antenna movement. Using the shorthand $\tau = mT_s$ and $p = p\Delta d$, the discrete UWB channel model in (3) becomes

$$h(p, \tau) = \sum_{i=0}^{L-1} \alpha_i(p) \delta(\tau - \tau_i(p)). \tag{4}$$

2.2. UWB Channel Measurement

In this work, real UWB-CIRs were collected from the time-domain UWB channel measurements to evaluate the performance of the proposed prediction method. The time-domain measurements were conducted in an outdoor environment considering line-of sight (LOS) scenarios using a pair of PulsON® 410 transceivers. Each transceiver had a vertically polarized omnidirectional wide-band dipole antenna mounted on it with operating frequencies of 3.1 to 10.6 GHz. The heights of the transmitter (Tx) and receiver (Rx) antennas were set to 2 m and 1.7 m, respectively. In our measurement

setup, a pulse bandwidth of 2.2 GHz over the frequency range of 3.1–5.3 GHz was used. The Rx was locked at 61 ps to capture the signal transmitted by the Tx. The measurements occurred in front of the Wireless Communication Center, Universiti Teknologi Malaysia, as depicted in Figure 1. This outdoor environment consisted of a concrete floor, wooden column roofing, and a parking space with several cars. The choice of this environment was done to illustrate an infostation scenario [37,38], where users can download data as they move along the corridor. Throughout this measurement, the Rx was located at a fixed position in front of the metallic sheet. This metallic sheet was placed between the person operating the setup and the setup itself to ensure a stationary environment. The Tx was then positioned along a straight line away from the Rx, which is marked by the white tape in Figure 1. The channel realization was captured starting at a Tx–Rx separation distance of $d = 3$ m and at each $\triangle d = 1$ cm transmitter movement away from the Rx. The final channel realization was captured at a separation distance of $d = 4.26$ m. As a result, the measurement campaign contained $P = 127$ sets of measurement data corresponding to all the Tx–Rx separation distances.

Figure 1. Channel Measurement Setup.

2.3. UWB Channel Impulse Response Extraction

In this section, we elaborate the process of extracting the UWB channel impulse response (CIR) from the measurement waveforms. $q(p)$ denotes the template waveform sent by the Tx at the p location index, and the delayed received waveform $r(p, \tau)$ after propagating through the channel $h(p, \tau)$ of (4) becomes

$$r(p, \tau) = q(p) \otimes h(p, \tau), \tag{5}$$

where $\otimes$ denotes the convolution operator. The channel analysis tool (CAT) integrated into the PulsON® 410 platform was used to log and capture the received UWB radio frequency (RF) waveforms in CAT logfile format (.csv file), which is compatible for processing using MATLAB. To obtain a high-resolution CIR, the received waveform can be further processed using the CLEAN algorithm [39]. The CLEAN algorithm is capable of resolving dense multipath components (MPCs) that are usually irresolvable by the conventional inverse filter, by deploying an iterative, high-resolution, and subtractive deconvolution procedure. To obtain $h(p, \tau)$ from $r(p, \tau)$, the CLEAN algorithm correlates the received waveform $r(p, \tau)$ with a template waveform $q(p)$, finds the highest correlation, assigns a weight, and then subtracts the template waveform from the received waveform [16,40]. This process is repeated until the maximum iterations expire or when an MPC with gain of a certain threshold value below the strongest MPC is detected. A 20 dB threshold value is recommended by the International Telecommunication Union-Radiocommunication (ITU-R) [41].

3. Window-Based UWB Channel Impulse Response Proposed Model

The significant transmission bandwidth of UWB systems enables a fine-grained delay resolution at the receiver. In many environments, only some of the resolvable delay bins carry significant multipath energy, yielding a sparse channel structure. To exploit this sparse structure, our model starts by grouping the delay bins of the channel impulse response using W non-overlapping windows. Next, a channel tap selection procedure, named the maximum tap gain selection, is used to choose the channel taps within the delay bins of each window. By implementing the proposed selection procedure, each window is represented using only one tap, hence, reducing and simplifying the original L taps sparse CIR of $h(p,\tau)$ in (4) with an approximated CIR of lower W taps.

3.1. Window Selection

We further elaborated the process of grouping the delay bins (i.e., channel taps) of UWB CIR using W non-overlapping windows, which can be written as

$$h(p,\tau) = \sum_{w=1}^{W} h_w(p,\tau). \tag{6}$$

In general, the first delay bin of $h(p,\tau)$ in (4) contains the LOS component (i.e., LOS channel path), while the remaining $L-1$ delay bins carry the MPCs. Hence, $h(p,\tau)$ can be divided into

$$\begin{aligned} h(p,\tau) &= h_{LOS}(p,\tau) + h_{MPC}(p,\tau) \\ &= \alpha_0(p)\delta(\tau-\tau_0(p)) + \sum_{i=1}^{L-1} \alpha_i(p)\delta(\tau-\tau_i(p)). \end{aligned} \tag{7}$$

To maintain the channel information of the LOS channel component, the size of the first window is always set to one delay bin to represent $h_{LOS}(p,\tau)$. Regarding the remaining $L-1$ delay bins, by grouping S delay bins into one window that generate the $W-1$ MPCs windows, where $W-1 = \lceil \frac{L-1}{S} \rceil$, $h_{MP}(p,\tau)$ can be divided using $W-1$ windows given by

$$h_{MP}(p,\tau) = \sum_{w=2}^{W-1} h_{MPC}^{(w)}(p,\tau) + h_{MPC}^{(W)}(p,\tau), \tag{8}$$

where $h_{MP}^{(w)}(p,\tau)$ for windows $w = \{2,3,\ldots,W-1\}$ contains S channel taps, and $h_{MPC}^{(W)}(p,\tau)$ for the last window contains the remaining $L-1-S(W-2)$ channel taps. Using (7) and (8) in (6), the CIR of UWB channels of (4) can be grouped into W non-equal and non-overlapping windows as follows:

$$\begin{aligned} h(p,\tau) &= \sum_{i=1}^{W} h_w(p,\tau) \\ &= h_{LOS}(p,\tau) + \sum_{w=2}^{W-1} h_{MPC}^{(w)}(p,\tau) + h_{MPC}^{(W)}(p,\tau), \end{aligned} \tag{9}$$

where

$$\begin{aligned} h_1(p,\tau) &= h_{LOS}(p,\tau) = \alpha_0(p)\delta(\tau-\tau_0(p)). && (10)\\ h_w(p,\tau) &= h^{(w)}_{MPC}(p,\tau) \\ &= \alpha_{1+S(w-2)}(p)\delta(\tau-\tau_{1+S(w-2)}(p))+\dots \\ &+ \alpha_{S+S(w-2)}(p)\delta(\tau-\tau_{S+S(w-2)}(p)), \quad \text{for } w=\{2,3,\dots,W-1\}. && (11)\\ h_W(p,\tau) &= h^{(W)}_{MPC}(p,\tau) \\ &= \alpha_{2+S(W-2)}(p)\delta(\tau-\tau_{2+S(W-2)}(p))+\alpha_{3+S(W-2)}(p)\delta(\tau-\tau_{3+S(W-2)}(p)) \\ &+ \dots+\alpha_{L-2}(p)\delta(\tau-\tau_{L-2}(p))+\alpha_{L-1}(p)\delta(\tau-\tau_{L-1}(p)). && (12) \end{aligned}$$

Here, the first multipath LOS component is placed in the first window as given in (10). In (11), the next multipath components are grouped using windows 2 to W-1, where each window has the same bin size of S. As an example, if (11) is used for window 3 (i.e., w = 3) and bin size of 10, the multipath components is $h_2(p,\tau) = \alpha_{1+10}(p)\delta(\tau-\tau_{1+10}(p)) + ... + \alpha_{S+10}(p)\delta(\tau-\tau_{S+10}(p))$. Finally, the remaining $L-1-S(W-2)$ multipath components are grouped using the last window, given by (12).

3.2. Channel Tap Selection

As previously explained, once the delay bins have been grouped using windows, the next step is to approximate the channel taps within each window by using only one tap. This process requires the generation of two new parameters to represent the one channel tap of each window, i.e., the tap gain $\bar{\alpha}_w(p)$ and delay $\bar{\tau}_w(p)$ for $w \in \{1,2,\dots,W\}$. Using these parameters, the CIR of (4) can be approximated using

$$h(p,\tau) \approx \bar{h}(p,\tau) = \sum_{w=1}^{W} \bar{\alpha}_w(p)\delta(\tau-\bar{\tau}_w(p)). \quad (13)$$

In this subsection, the tap selection approach is proposed to compute $\bar{\alpha}_w(p)$ and $\bar{\tau}_w(p)$. This approach is called maximum tap gain selection, where a significant path with maximum tap gain is selected from each of the windows to approximate the sparse CIR of UWB channels. Under this approach the maximum tap gain $\bar{\alpha}_w(p)$ for each window is given by

$$\begin{aligned} |\alpha_0(p)|, &\quad \text{for } w=1 \\ \max\{|\alpha_{1+S(w-2)}(p)|,\dots,|\alpha_{S+S(w-2)}(p)|\}, &\quad \text{for } w=2,\dots,W-1 \\ \max\{|\alpha_{2+S(W-2)}(p)|,|\alpha_{3+S(W-2)}(p)|,\dots,|\alpha_{L-1}(p)|\}, &\quad \text{for } w=W \end{aligned}$$

The delay of proposed window models is presented in two approaches. The first approach is to use the delay bin of the selected channel path with the maximum tap gain in each window, termed $\bar{\tau}_w(p)$. The proposed tap selection is called the windowing-based on bin delay (WB-BD) approach. For further simplification, in the second approach, the delay parameter is set to the delay of the last bin in each window and termed $\bar{\tau}_{w,1}(p)$. We call this approach the windowing-based on window delay (WB-WD) approach, where the delay parameter is the window size delay defined as

$$\bar{\tau}_{w,1}(p) = \begin{cases} \tau_0(p), & \text{for } w=1 \\ \tau_{S+S(w-2)}(p), & \text{for } w=2,\dots,W-1 \\ \tau_{L-1}(p), & \text{for } w=W. \end{cases}$$

Representing the delay parameters with the window size delay standardizes the approximated CIRs at all location indexes p with similar bin sizes, hence simplifying the prediction of the delay parameters for future CIRs.

4. Channel Impulse Response Tap Prediction Algorithms

This section explains the time-domain prediction strategies that are used to predict the evolution of the UWB CIR tap. Specifically, the RLS algorithm is used to predict the simplified CIR tap of UWB channels. The aim of the prediction strategies is to predict the CIR taps associated with the future transmitted symbols, given the previous CIR taps is considered. Hence, the problem of predicting the CIR at the index $p+1$ given the measured CIRs for spatial locations at indices $1, 2, \ldots, p$. Based on the proposed and simplified CIR using windows, two parameters must be predicted to obtain the CIR at index $p+1$, i.e., the tap gain $\bar{\alpha}_w(p+1)$ and the delay $\bar{\tau}_w(p+1)$ for the WB-BD approach. However, the delay parameters do not need to be predicted for the WB-WD approach. In this work, the fading process of the simplified CIR is modeled as an autoregressive process (AP) of the order $p_1 \leq p$, and the estimate of both tap gain and delay parameters can be obtained using

$$\bar{\alpha}_w(p+1) = \underline{C}^H_{\bar{\alpha},w}(p) \cdot \underline{\bar{\alpha}}_w(p) \quad (14)$$

$$\bar{\tau}_w(p+1) = \underline{C}^H_{\bar{\tau},w}(p) \cdot \underline{\bar{\tau}}_w(p) \quad (15)$$

where $\underline{C}_{\bar{\alpha},w}(p) = (C_{\bar{\alpha},w}[1], \ldots, C_{\bar{\alpha},w}[p_1])^T$ is the prediction filter coefficient vector for the channel tap gain, and $\underline{C}_{\bar{\tau},w}(p) = (C_{\bar{\tau},w}[1], \ldots, C_{\bar{\tau},w}[p_1])^T$ is the filter coefficient for the channel delay. We define $\underline{\bar{\alpha}}_w(p) = (\bar{\alpha}_w(p), \ldots, \bar{\alpha}_w(p-p_1+1))^T$ and $\underline{\bar{\tau}}_w(p) = (\bar{\tau}_w(p), \ldots, \bar{\tau}_w(p-p_1+1))^T$.

The superscripts T and H denote the transpose and Hermitian transpose operators, respectively. Here, the RLS algorithm is considered to adaptively compute the coefficients of the prediction filters in (14) and (15).

Under the RLS algorithm, the predictor filter $\underline{C}_{A,w}(p)$ for $A \in \{\bar{\alpha}, \bar{\tau}\}$ can be computed by minimizing the following cost function:

$$\beta_{A,RLS}(p) = \sum_{i=1}^{p} \lambda_A^{p-i} \cdot |A_{w,i}(p+1) - \underline{C}^H_{A,w}(p) \cdot \underline{A}_{w,i}(p)|^2. \quad (16)$$

Here, λ_A is the forgetting factor. In this work, we set λ_A to 1. The resulting RLS update equation for $\underline{C}_{A,w}(p)$ is

$$\underline{C}_{A,w}(p) = \underline{C}_{A,w}(p-1) + \underline{G}_{A,w}(p-1) \cdot e^*_{A,w}(p) \quad (17)$$

where the prediction error $e^*_{A,w}(p)$ can be computed by

$$e^*_{A,w}(p) = A_{w,i}(p) - \underline{C}^H_{A,w}(p-1) \cdot \underline{A}_{w,i}(p-1). \quad (18)$$

Then, the RLS gain vector in (17) is

$$\underline{G}_{A,w}(p-1) = \frac{\underline{R}_{A,w}(p-1)\underline{A}_{w,i}(p)}{\lambda + \underline{A}^H_{w,i}(p)\underline{R}_{A,w}(p-1)\underline{A}_{w,i}(p)} \quad (19)$$

where matrix $\underline{R}_{A,w}(p)$ denotes the inverse of the w-th CIR taps of $p_1 \times p_1$ dimensional sample covariance matrix, which can be computed recursively using

$$\underline{R}_{A,w}(p) = \lambda_A^{-1} \times \left(\mathrm{I}_p - \underline{G}_{A,w}(p)\underline{A}^H_{w,i}(p)\right) \times \underline{R}_{A,w}(p-1), \quad (20)$$

where I_p is the $p \times p$ identity matrix.

5. Evaluation Criterion

The proposed windowing-based UWB-CIR models and prediction techniques were evaluated by comparing the mean square error (MSE) of the waveform obtained from measurement campaigns with the waveform reconstructed using the modeled and predicted CIRs. The reconstructed waveform was generated by convolving the template pulse $q(p)$ with the modeled and predicted CIRs. By denoting the measured received waveform by $r(p,\tau)$ in (4), the reconstructed waveform from the modeled CIR by $r_m(p,\tau)$ and from the predicted CIR by $r_p(p,\tau)$, the MSE between the measured and reconstructed waveform is given by

$$E(p) = \frac{1}{K}\sum_{i=1}^{K}\Big(r(p,\tau) - r_i(p,\tau)\Big)^2 \tag{21}$$

for $i \in \{m,p\}$, and K is the total number of samples in the received waveform. To evaluate the proposed method at L location indices, the average MSE is given by

$$E_{1avg} = \frac{\sum_{p=1}^{L} E(p)}{L}. \tag{22}$$

The proposed UWB-CIRs models were also evaluated from the perspective of time dispersion characteristics given by the RMS delay spread parameter [42]

$$\tau_{rms} = \sqrt{\frac{\sum_l P_l \cdot (\tau_l - \tau_b - \tau_m)^2}{\sum_l P_l}}, \tag{23}$$

where τ_{rms} is the RMS delay spread that is defined by the square root of the second central moment of a power delay profile (PDP), P_l is the power for the l-th path, τ_l is the arrival time of the MPCs, τ_b is the first path arrival time, and τ_m is the mean excess delay that can be represented by the first moment of the PDP as

$$\tau_m = \frac{\sum_l P_l \cdot (\tau_l - \tau_b)}{\sum_l P_l}. \tag{24}$$

6. Complexity Analysis

This section discusses the computational complexity of our proposed windowing-based CIR models under RLS prediction algorithms, expressed by the number of basic operations (i.e., addition, division, and multiplication). Table 1 presents the computational cost of the RLS algorithm per iteration [43]. For the standard UWB-CIR with L delay bins and M prediction order, the prediction requires $L(M^2+5M+1)$ multiplication, $L(M^2+3M)$ addition, and L division operations per iteration. Here, prediction is required for every delay bin, even though it does not contain any MPCs. By utilizing the sparsity of the UWB-CIR, the proposed UWB-CIR models use a lower number of W bins, i.e., $W < L$. For the WB-BD model, the prediction of the channel tap gain and its delay parameter is required. As a result, the WB-BD approach requires $2W(M^2+5M+1)$ multiplication, $2W(M^2+3M)$ addition, and $2W$ division operations per iteration. For the WB-WD model, prediction for the delay parameter is not required as this value is further approximated to the window bin delay. Thus, the complexity of the WB-WD model is halved compared to that of WB-BD model. Here, both WB-BD and WB-WD models use fewer W bins to achieve a reduction in complexity by factors of $L/(2W)$ and L/W, respectively, over the standard CIR model with L bins. Note that, even though the complexity analysis is performed using the RLS algorithm, the reduction in prediction complexity is achieved by adopting simplified UWB-CIR models. Hence, the models will also simplify prediction methods utilizing different algorithms.

Table 1. Computational cost of the recursive least square (RLS) algorithm per iteration [43].

Operation	×	+	/
$e^*_{A,w}(p)$	M	M	
$A^H_{w,i}(p)\underline{R}_{A,w}(p-1)$	$M(M+1)$	$M(M-1)$	
$A(p)\underline{R}_{A,w}(p-1)\underline{A}_{w,i}(p)$	M	$M-1$	
$\lambda + \underline{A}^H_{w,i}(p)\underline{R}_{A,w}(p-1)\underline{A}_{w,i}(p)$		1	
$\underline{R}_{A,w}(p)$		M	
$\underline{R}_{A,w}(p-1)\underline{A}_{w,i}(p)$	M		
$\underline{G}_{A,w}(p-1)$	1		1
$\underline{G}_{A,w}(p-1).e^*_{A,w}(p)$	M		
$\underline{C}_{A,w}(p)$		M	
Total cost per iteration	M^2+5M+1	M^2+3M	1

7. Results and Discussion

This section presents the modeling and prediction MSE performances along with the statistical properties of the RMS delay spread for the proposed windowing-based CIR models.

7.1. Modeling Results

Before discussing the prediction performance, we first present results to show the impact of reducing the number of MPCs to the CIR when adopting our proposed windowing-based models in terms of both the MSE and the RMS delay spread parameter. Figure 2 presents the received waveform $r(p,\tau)$ at a Tx–Rx separation distance of 4.07 m. Using this $r(p,\tau)$ measured waveform, several CIRs were extracted by using different approaches and are depicted in Figure 3. As a benchmark, Figure 3a represents the CIR extracted by the CLEAN algorithm with the ITU-R recommended threshold of 20 dB (CA-ITUR20dB). The CA-ITUR20dB CIR is very sparse; there are 380 resolution delay bins with only 23 non-zero MPCs. Note that, although there are only 23 MPCs, the prediction for CIR coefficients in the next time slot must be performed within all 380 delay bins because the locations of these MPCs are random within the delay bins. Lowering the threshold of the CLEAN algorithm reduced the channel gain gap between the strongest and weakest MPCs of the CIR, hence reducing the number of MPCs. As a result, a CLEAN algorithm with different thresholds (CA-WDT) can be used to generate CIRs with different number of MPCs. Figure 3b,c show two CIRs with reduced 9 and 7 MPCs extracted by the CLEAN algorithm with lower 15 dB and 10 dB thresholds, respectively. Despite the reduction in the number of MPCs, the complexity of channel prediction for these CIRs was similar to the CIR of the CA-ITUR20dB approach, i.e., all zero and non-zero MPCs in 380 delay bins must be predicted because their time delay parameters are random. Finally, Figure 3d shows the CIR with similar 7 MPCs when utilizing our proposed WB-BD model. We can see that the proposed WB-BD CIR in Figure 3d is more structured when compared to the CIR of CA-WDT of 10 dB in Figure 3c; this structure provides benefit to certain applications, such as channel prediction.

Let us now compare the modeling average the MSE results for the windowing-based models with the CA-ITUR20dB and CA-WDT approaches. These results are shown in Figure 4. We see that the CIR from CA-ITUR20dB approach showed the lowest MSE as a result of having the most MPCs. We can also see that the average MSE started to increase when the number of MPCs reduced for the CA-WDT approach and the windowing-model CIRs. For a fair comparison, a similar number of MPCs was set for CIR in both the windowing-based models and the CA-WDT approach. The number of MPCs was determined by setting the threshold of the CLEAN algorithm and the window size (which is defined by the number of bin per window (bpw)) for the CA-WDT approach and windowing-based models, respectively. The CIR of the CA-WDT approach introduced the lowest increment in average MSE when compared to CA-ITUR20dB. However, the average MSE increment for the proposed WB-BD model can still be considered small and acceptable for 25 bpw and lower. In contrast, the CIR of the WB-WD model showed significant increases in the average MSE compared with the other three CIRs. The MSEs

of the WB-WD model were approximately 7 and 8 times larger than the benchmark CA-ITUR20dB for 5 and 35 bpw, respectively.

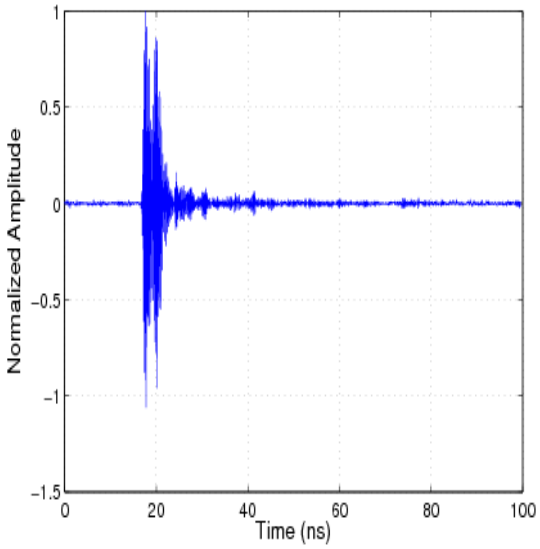

Figure 2. Received waveform at the Tx–Rx separation distance of a 4.07 m.

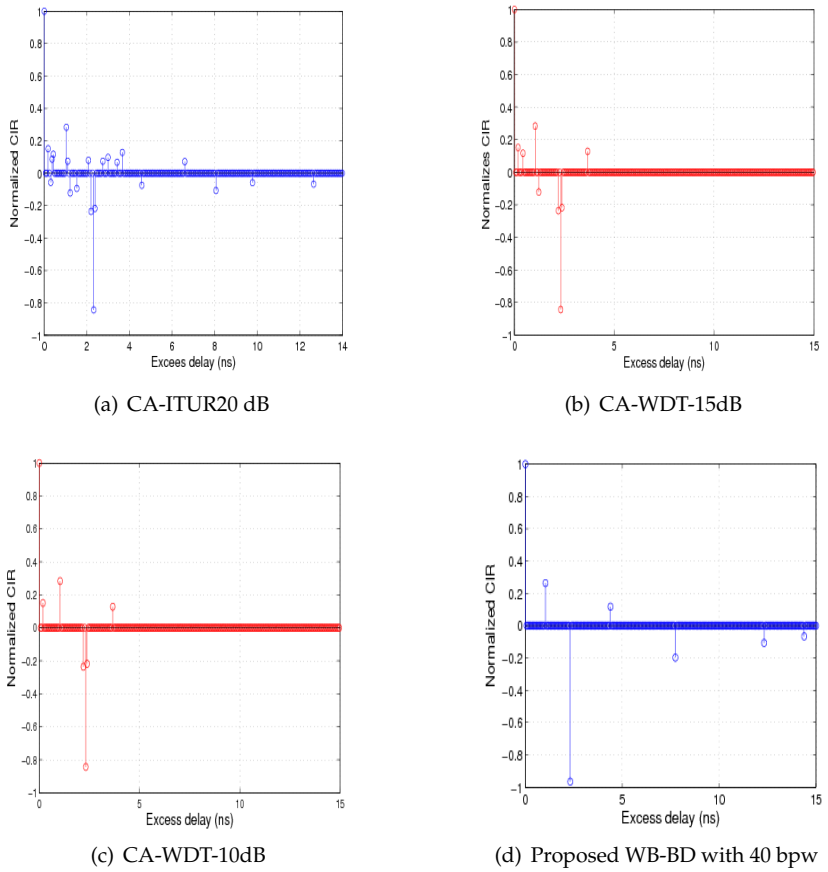

(a) CA-ITUR20 dB (b) CA-WDT-15dB

(c) CA-WDT-10dB (d) Proposed WB-BD with 40 bpw

Figure 3. Comparison of channel impulse response (CIR) samples at the Tx–Rx separation distance of 4.07 m (**a**) CA-ITUR20dB, (**b**) CA-WDT-15dB, (**c**) CA-WDT-10dB, and (**d**) the proposed WB-BD model.

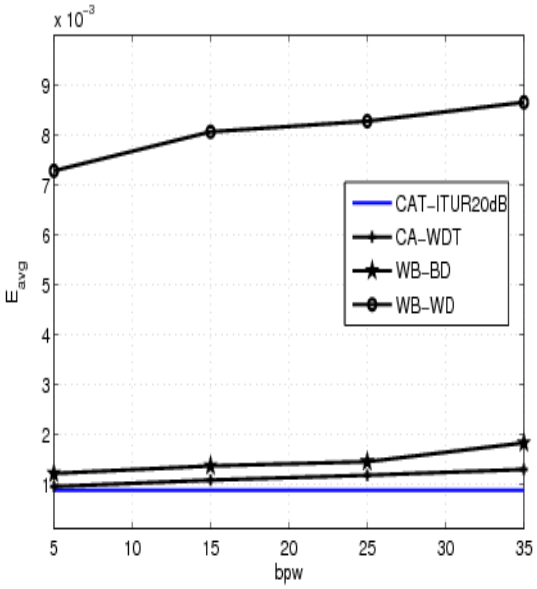

Figure 4. The modeling mean square error (MSE) for windowing-based on bin delay (WB-BD), windowing-based on window delay (WB-WD), CA-WDT and CA-ITUR20dB CIRs.

Figure 5 presents the RMS delay spread values for the windowing-based models with different window sizes, generated using the measured CIR at a Tx–Rx separation distance of 3.57 m. The RMS delay spread of 1.98 ns for the CIR of CA-ITUR20dB approach was used as a benchmark to determine how the RMS delay spreads of our proposed models deviate from the original CIR of CA-ITUR20dB. The RMS delay spread of the WB-BD model was slightly higher than the one achieved by CA-ITUR20dB—approximately 2.00 ns for window sizes of 5 to 25 bpw. The RMS delay spread of the WB-BD model then decreased to 1.98 ns at 30 bpw, similar to the result of the benchmarked CA-ITUR20dB. The results show that our proposed WB-BD CIR model with lower number of MPCs has a very small impact on the statistics of RMS delay spread. Hence, the system transmission rate is not impacted when adopting this less complex WB-BD CIRs. Regarding the results of WB-WD model in Figure 5, the RMS delay spread increased with the window size in the range between 2.01 and 2.65 ns for 5 and 35 bpw, respectively. The increased of RMS delay spread value reduced the system transmission rate if it was larger than the inverse of the system bandwidth. In Figure 5, the WB-WD CIR with 35 bpw has a RMS delay spread of 2.65 ns, which is 0.67 ns greater than the RMS delay spread of the benchmark CA-ITUR20dB and higher than the tolerable system inverse bandwidth of 0.45 ns. When adopting the simplified WB-WD CIR with 35 bpw, this increased of RMS delay spread by 0.22 ns above the tolerable inverse system bandwidth reduces the system transmission rate by approximately 30% when compared to the communication system utilizing the CIR of CA-ITUR20dB.

Next, Figure 6 presents the values of RMS delay spread for the windowing-based models with different window sizes generated using another measured CIR at a Tx–Rx separation distance of 3 m. A similar RMS delay spread pattern of values can be observed as the results shown in Figure 5 for a Tx–Rx separation distance of 3.57 m. Here, the RMS delay spread of CA-ITUR20dB was shown to be 1.53 ns, which is comparable to the values achieved by our proposed WB-BD model. For the CIR of the WB-WD model, the RMS delay spread values varied between 1.57 and 2.25 ns for 5 and 35 bpw, respectively. The RMS delay spread for the WB-WD model with 35 bpw was approximately 0.72 ns greater than the CA-ITUR20dB approach and 0.27 ns higher than the tolerable inverse system bandwidth of 0.45 ns. This higher RMS delay spread reduced the system transmission rate by approximately 36% when compared to the communication system utilizing the CIR of CA-ITUR20dB.

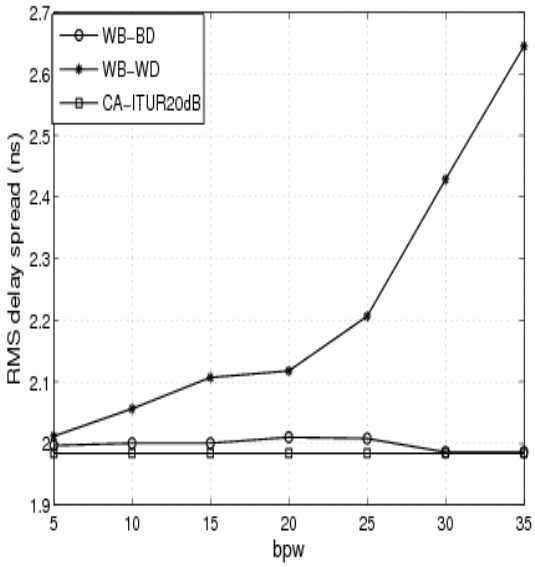

Figure 5. RMS delay spread for different window sizes at the Tx–Rx separation distance of 3.57 m.

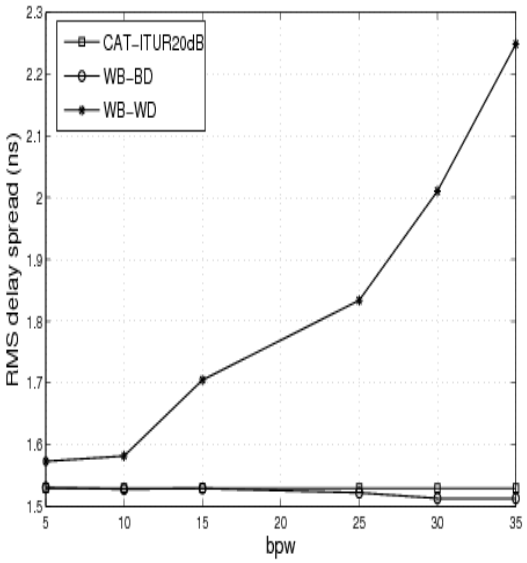

Figure 6. RMS delay spread for different window sizes at the Tx–Rx separation distance of 3 m.

7.2. Prediction Results

We present the prediction performances, i.e., the average MSE of (22), resulting from the adoption of the windowing-based models. For prediction order $M = 5$, the CIR at the Tx–Rx location index of 3.05 was predicted by the RLS algorithm utilizing measured CIRs from the 5 previous Tx–Rx location indices of 3.0 m to 3.04, and then, the MSE of (21) was computed. Here, the average MSE of (22) for $M = 5$ in our plot was obtained by averaging the MSE values of (21) computed from predicting the CIRs at 122 location indices of 3.05 m up to 4.26 m. The average predicted MSEs under the RLS algorithm utilizing CIRs for the benchmarked CA-ITUR20dB are shown in Figure 7. For predictions using the CA-ITUR20dB CIRs, the channel tap gains in all 380 delay bins must be predicted. We see that the average MSE of CA-ITUR20dB model improved when higher prediction orders of the RLS algorithm were applied. Figure 7 also shows the average prediction MSE for our proposed WB-BD models using 5, 15, 25 and 35 bpw. We see that the average prediction MSE value adopting the WB-BD models increased with the window size because increasing the window size reduces the number of MPCs of the WB-BD CIRs. For $M = 20$, the average MSEs for CIR prediction utilizing WB-BD models

of 5, 15, 25 and 35 bpw were approximately 1.25×10^{-3}, 1.37×10^{-3}, 1.5×10^{-3}, and 1.87×10^{-3}, respectively. In general, the average MSE for CIR prediction adopting the WB-BD model improved with the prediction order; this improvement decreased when a higher window size was used. For example, the average MSE for the window size of 35 bpw remained comparable at approximately 1.87×10^{-3}, even at higher prediction orders, and for the window size of 5 bpw, the average MSE improved from approximately 1.35×10^{-3} for $M = 5$ to 1.25×10^{-3} for $M = 30$. The main advantage of the proposed WB-BD model for prediction is the reduction in computational complexity via the lower number of MPCs. As shown in Figure 7, our proposed WB-BD models not only requires a lower prediction complexity, but it also outperforms the benchmarked CA-ITUR20dB CIR at the lower prediction order region. For example, when considering the RLS prediction order $M = 5$, the WB-BD model with 25 bpw achieved a lower average MSE of 1.5×10^{-3}, whereas the CA-ITUR20dB model achieved a higher average MSE of approximately 1.77×10^{-3}. Here, the proposed WB-BD model achieved a 15% lower prediction error rate with a prediction complexity reduction factor of 12, because at 25 bpw, the simplified WB-BD CIR is represented by only 15 MPCs.

Next, Figure 8 presents the average prediction MSEs under the RLS algorithm utilizing CIRs from the WB-WD models for different window sizes of 5, 15, 25, and 35 bpw. By approximating the time delay parameters to the window size using the proposed WB-WD models, the prediction complexity reduced further by a factor of 2 when compared to the WB-BD models; however, this reduced complexity slightly degraded the prediction performances. For the comparison at the prediction order of 20 and a window size of 15 bpw, the average MSE of the WB-WD model in Figure 8 was approximately 7.8×10^{-3}, and the average MSE for the WB-BD model in Figure 7 was approximately 1.38×10^{-3}.

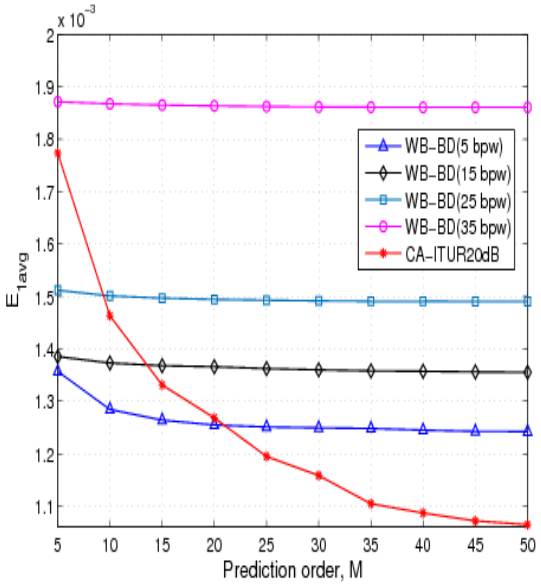

Figure 7. The prediction mean square error (MSE) for different window sizes and prediction orders of the WB-BD approach.

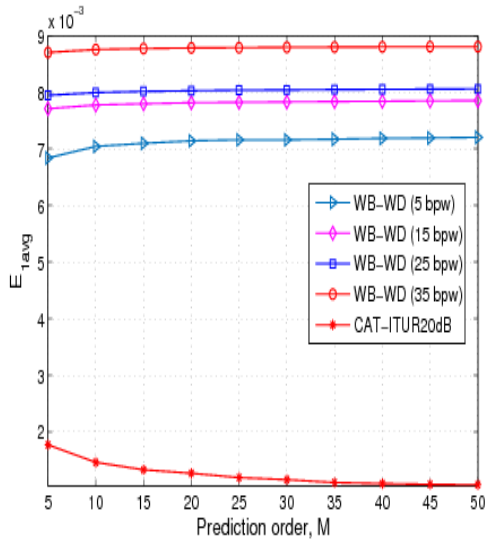

Figure 8. The prediction mean square error (MSE) for different window sizes and prediction orders of WB-WD approach.

7.3. CDF of RMS Delay Spread

Next, we considered the RMS delay spread distribution for the proposed WB-BD and WB-WD models. First we considered the distribution of the modeled windowing-based approaches. Figure 9 shows the cumulative density function (CDF) comparing the RMS delay spreads for the WB-BD and CA-ITUR20dB models. We found that the distribution of RMS delay spreads for the WB-BD model using 5, 15, and 25 bpw were comparable with the CIR of CA-ITUR20dB. This finding implies that the simplified WB-BD model maintains the second-order characteristics of the UWB channels. The CDF of the RMS delay spreads for the second WB-WD model is depicted in Figure 10. Note that, by further approximation of the time delay parameter with the window size, the CDF of RMS delay spreads for the WB-WD CIRs deviated from the CA-ITUR20dB model. This deviation increased with an increased window size. Here, 90% of the RMS delay spread values for CIRs of CA-ITUR20dB were lower than 1.9 ns, and 90% of the RMS delay spreads of the WB-WD CIRs were below 2 ns, 2.1 ns, and 2.2 ns for the window sizes of 5, 15, and 25 bpw, respectively.

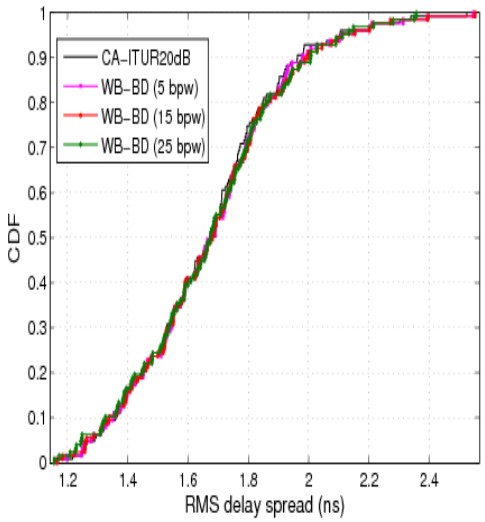

Figure 9. Cumulative density function (CDF) of the RMS delay spread for the modeled WB-BD CIRs.

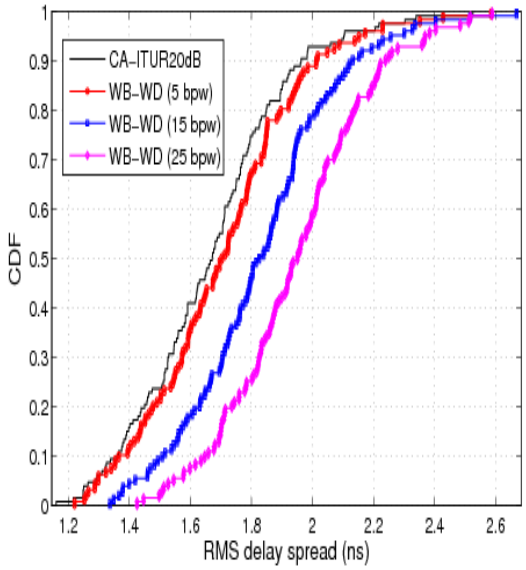

Figure 10. CDF of the RMS delay spread for the modeled WB-WD CIRs.

We then considered the distributions of the RMS delay spreads for the predicted CIRs using the WB-BD and CA-ITUR20B models. Figure 11 shows the CDFs of the RMS delay spreads for the predicted CIRs using the RLS algorithm with $M = 10$ for the WB-BD and CA-ITUR20dB models. Here, only the CDFs of delay spreads for the WB-BD models with 5 and 15 bpw were considered because they have lower average prediction MSE values than the CA-ITUR20dB model. The delay dispersion has great importance for high-data rate systems, where the error probability due to delay dispersion is proportional to the RMS delay spread. Figure 11 shows that 90% of RMS delay spreads utilizing the proposed WB-BD models with 5 and 15 bpw were less than 1.6 ns. For the CA-ITUR20dB models, 90% of the RMS delay was less than 2.0 ns. The results show that the predicted CIRs using the WB-BD models with 5 and 15 bpw not only improved the prediction performance but also reduced their delay dispersions provided by the RMS delay spreads compared to the predicted CIRs using the CA-ITUR20dB model.

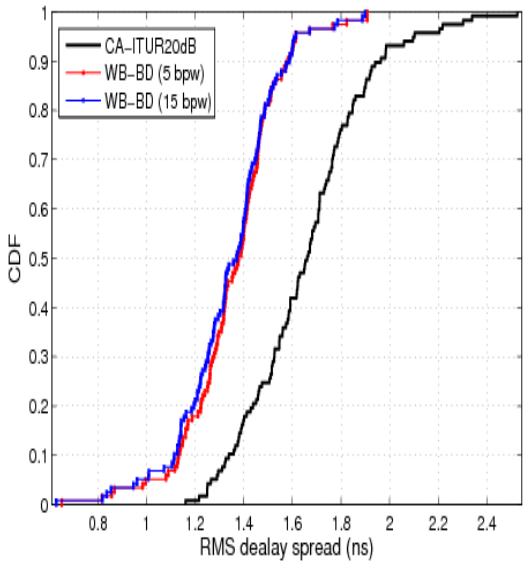

Figure 11. CDF of the RMS delay spread for the predicted CIRs using the recursive least square (RLS) algorithm with M = 10.

8. Conclusions

This paper applied real CIRs collected from measurement campaigns in an outdoor environment to investigate a time-domain based channel prediction for UWB channels. A less complex and simplified CIR prediction method involving the exploitation of the sparse property of UWB channels was proposed by introducing two new models: the WB-BD and WB-WD UWB-CIR models. The new models were generated by grouping channel taps of ITU-R UWB-CIRs with a 20 dB threshold using non-overlapping windows, and consequently, two procedures were introduced to select channel taps within each window. The MSE performances and RMS delay spread values were used to evaluate the proposed methods. Based on the modeling and predicted MSE performances, the WB-BD model outperformed the WB-WD model. Based on RLS algorithms, the channel prediction utilizing the WB-BD model was shown to outperform not only the WB-WD model, but it also achieved a 15% lower prediction error rate with a reduction factor of 12 in the prediction complexity over the ITU-R UWB-CIR. In addition to the lower prediction performance and complexity when using the WB-BD model, the predicted CIRs were found to possess smaller RMS delay spread values. These results highlight the potential of the UWB WB-BD channel model for critical applications such as the future 5G systems requiring both high data rate and low-latency.

Author Contributions: All authors contributed equally to this paper.

Funding: Research Management Centre (RMC) at Universiti Teknologi Malaysia: Q.J130000.21A2.04E21, UTM research grant (Vot 4J218), Universiti Teknologi Malaysia

Acknowledgments: We would like to thank the Research Management Centre (RMC) at Universiti Teknologi Malaysia for funding this work under grant number Q.J130000.21A2.04E21. Also, the authors would like to acknowledge UTM research grant (Vot 4J218), Universiti Teknologi Malaysia.

Conflicts of Interest: The authors declare no conflict of interest.

References

1. Benedetto, M.G.D.; Kaiser, T.; Molisch, A.F.; Oppermann, I.; Politano, C.; Porcino, D. *UWB Communications Systems: A Comprehensive Overview (EURASIP Book Series on Signal Processing and Communications)*; Hindawi Publishing Corporation: New York, NY, USA, 2006.
2. Yang, L.; Giannakis, G. Ultra-wideband communications: An idea whose time has come. *IEEE Signal Process. Mag.* **2004**, *21*, 26–54. [CrossRef]
3. Roy, S.; Foerster, J.; Somayazulu, V.; Leeper, D. Ultrawideband radio design: The promise of high-speed, short-range wireless connectivity. *Proc. IEEE* **2004**, *92*, 295–311. [CrossRef]
4. Molisch, A. Ultrawideband propagation channels-theory, measurement, and modeling. *IEEE Trans. Veh. Technol.* **2005**, *54*, 1528–1545. [CrossRef]
5. FCC Notice of Proposed Rule Making, Revision of Part 15 of the Commission's Rules Regarding Ultra-Wideband Transmission Systems; ET-Docket; 2005; pp. 98–153. Available online: https://www.fcc.gov/document/revision-part-15-commissions-rules-regarding-ultra-wideband-transmission-systems-2 (accessed on 1 October 2018).
6. Tsiropoulou, E.E.; Kapoukakis, A.; Papavassiliou, S. Uplink resource allocation in SC-FDMA wireless networks: A survey and taxonomy. *Comput. Netw.* **2016**, *96*, 1–28. [CrossRef]
7. Myung, H.G.; Lim, J.; Goodman, D.J. Single carrier FDMA for uplink wireless transmission. *IEEE Veh. Technol. Mag.* **2006**, *1*, 30–38. [CrossRef]
8. Tsiropoulou, E.E.; Kapoukakis, A.; Papavassiliou, S. Energy-efficient subcarrier allocation in SC-FDMA wireless networks based on multilateral model of bargaining. In Proceedings of the 2013 IFIP Networking Conference, Brooklyn, NY, USA, 22–24 May 2013; pp. 1–9.
9. Myung, H.G. Introduction to single carrier FDMA. In Proceedings of the 15th European Signal Processing Conference, Poznan, Poland, 3–7 September 2007; pp. 2144–2148.
10. Gustafson, C.; Haneda, K.; Wyne, S.; Tufvesson, F. On mm-Wave Multipath Clustering and Channel Modeling. *IEEE Trans. Antennas Propag.* **2014**, *62*, 1445–1455. [CrossRef]

11. Sulyman, A.I.; Alwarafy, A.; Maccartney, G.; Rappaport, T.; Al-Sanie, A. Directional Radio Propagation Path Loss Models for Millimeter-Wave Wireless Networks in the 28, 60, and 73 GHz Bands. *IEEE Trans. Wirel. Commun.* **2016**, *15*, 6939–6947. [CrossRef]
12. Andrews, J.; Buzzi, S.; Choi, W.; Hanly, S.; Lozano, A.; Soong, A.; Zhang, J. What Will 5G Be? *IEEE J. Sel. Areas Commun.* **2014**, *32*, 1065–1082. [CrossRef]
13. Li, Y.; Jin, Z.; Wang, Y. Adaptive Channel Estimation Based on an Improved Norm-Constrained Set-Membership Normalized Least Mean Square Algorithm. *Wirel. Commun. Mob. Comput.* **2017**, *2017*, 8056126. [CrossRef]
14. Molish, A.; Tufvesson, F. Propagation channel models for next-generation wireless communications systems. *IEICE Trans. Commun.* **2014**, *97*, 2022–2034. [CrossRef]
15. METIS ICT-317669-METIS/D1.1, S. Scenarios, Requirements and KPIs for 5G Mobile and Wireless System. Available online: www.metis2020.com (accessed on 1 October 2018).
16. Anderson, C.R.; Volos, H.I.; Buehrer, R.M. Characterization of Low-Antenna Ultrawideband Propagation in a Forest Environment. *IEEE Trans. Veh. Technol.* **2013**, *62*, 2878–2895. [CrossRef]
17. Cramer, R.M.; Scholtz, R.; Win, M. Evaluation of an ultra-wide-band propagation channel. *IEEE Trans. Antennas Propag.* **2002**, *50*, 561–570. [CrossRef]
18. Molisch, A.F. Ultra-Wide-Band Propagation Channels. *Proc. IEEE* **2009**, *97*, 353–371. [CrossRef]
19. Athanasiadou, G.; Nix, A. A novel 3-D indoor ray-tracing propagation model: The path generator and evaluation of narrow-band and wide-band predictions. *IEEE Trans. Veh. Technol.* **2000**, *49*, 1152–1168. [CrossRef]
20. Al-Samman, A.M.; Rahman, T.A.; Hadri, M.; Khan, I.; Chua, T.H. Experimental UWB Indoor Channel Characterization in Stationary and Mobility Scheme. *Measurement* **2017**, *111*, 333–339. [CrossRef]
21. Al-Samman, A.M.; Rahman, T.A.; Azmi, M.H.; Hindia, M.N.; Khan, I.; Hanafi, E. Statistical Modelling and Characterization of Experimental mm-Wave Indoor Channels for Future 5G Wireless Communication Networks. *PLoS ONE* **2016**, *11*, e0163034. [CrossRef] [PubMed]
22. Maccartney, G.R.; Rappaport, T.S.; Sun, S.; Deng, S. Indoor Office Wideband Millimeter-Wave Propagation Measurements and Channel Models at 28 and 73 GHz for Ultra-Dense 5G Wireless Networks. *IEEE Access* **2015**, *3*, 2388–2424. [CrossRef]
23. Rappaport, T.S.; MacCartney, G.R.; Samimi, M.K.; Sun, S. Wideband Millimeter-Wave Propagation Measurements and Channel Models for Future Wireless Communication System Design. *IEEE Trans. Commun.* **2015**, *63*, 3029–3056. [CrossRef]
24. Al-Samman, A.M.; Rahman, T.A.; Azmi, M.H.; Hindia, M. Large-scale path loss models and time dispersion in an outdoor line-of-sight environment for 5G wireless communications. *AEU—Int. J. Electron. Commun.* **2016**, *70*, 1515–1521. [CrossRef]
25. Gupta, A.; Jha, R.K. A Survey of 5G Network: Architecture and Emerging Technologies. *IEEE Access* **2015**, *3*, 1206–1232. [CrossRef]
26. Huo, Y.; Member, S.; Dong, X.; Member, S. 5G Cellular User Equipment : From Theory to Practical Hardware Design. *IEEE Access* **2017**, *5*, 13992–14010. [CrossRef]
27. Duel-Hallen, A. Fading channel prediction for mobile radio adaptive transmission systems. *Proc. IEEE* **2007**, *95*, 2299–2313. [CrossRef]
28. Al-Samman, A.M.; Nunoo, S.; Rahman, T.A.; Chude-Okonkwo, U.A.K.; Ngah, R. Hybrid Channel Estimation Technique with Reduced Complexity for LTE Downlink. *Wirel. Pers. Commun.* **2015**, *82*, 1147–1159. [CrossRef]
29. Heo, J.; Wang, Y.P.; Chang, K.H. A novel two-step channel-prediction technique for supporting adaptive transmission in OFDM/FDD system. *IEEE Trans. Veh. Technol.* **2008**, *57*, 188–193. [CrossRef]
30. Akhtman, J.; Hanzo, L. Channel Impulse Response Tap Prediction for Time-Varying Wireless Channels. *IEEE Trans. Veh. Technol.* **2007**, *56*, 2767–2769. [CrossRef]
31. Malmirchegini, M.; Mostofi, Y. On the Spatial Predictability of Communication Channels. *IEEE Trans. Wirel. Commun.* **2012**, *11*, 964–978. [CrossRef]
32. Jarinová, D. On autoregressive model order for long-range prediction of fast fading wireless channel. *Telecommun. Syst.* **2011**, *52*, 1533–1539. [CrossRef]
33. Wang, Y.; Li, Y. Sparse Multipath Channel Estimation Using Norm Combination Constrained Set-Membership NLMS Algorithms. *Wirel. Commun. Mob. Comput.* **2017**, *2017*, 8140702. [CrossRef]

34. Tsao, J.; Porrat, D.; Tse, D. Prediction and Modeling for the Time-Evolving Ultra-Wideband Channel. *IEEE J. Sel. Top. Signal Process.* **2007**, *1*, 340–356. [CrossRef]
35. Tse, D. *Fundamentals of Wireless Communication*; Cambridge University Press: Cambridge, UK, 2005.
36. Saleh, A.; Valenzuela, R. A Statistical Model for Indoor Multipath Propagation. *IEEE J. Sel. Areas Commun.* **1987**, *5*, 128–137. [CrossRef]
37. Santos, T.; Karedal, J.; Almers, P.; Tufvesson, F.; Molisch, A.F. Modeling the ultra-wideband outdoor channel: Measurements and parameter extraction method. *IEEE Trans. Wirel. Commun.* **2010**, *9*, 282–290. [CrossRef]
38. Nunoo, S.; Chude-Okonkwo, U.A.K.; Ngah, R.; Al-Samman, A.; Onubogu, J. UWB channel measurement and data transfer analysis for multiuser Infostation applications. In Proceedings of the 2014 IEEE 10th International Colloquium on Signal Processing and its Applications, Kuala Lumpur, Malaysia, 7–9 March 2014. [CrossRef]
39. Liu, T.K.; Kim, D.I.; Vaughan, R.G. A high-resolution, multi-template deconvolution algorithm for time-domain UWB channel characterization. *Can. J. Electr. Comput. Eng.* **2007**, *32*, 207–213. [CrossRef]
40. Chandra, A.; Blumenstein, J.; Mikulasek, T.; Vychodil, J.; Pospisil, M.; Marsalek, R.; Prokes, A.; Zemen, T.; Mecklenbrauker, C. CLEAN Algorithms for Intra-vehicular Time-domain UWB Channel Sounding. In Proceedings of the 2015 International Conference on Pervasive and Embedded Computing and Communication Systems (PECCS), Angers, France, 11–13 February 2015.
41. Propagation, M. *Multipath Propagation and Parameterization of Its Characteristics*; International Telecommunication Union: Geneva, Switzerland, 2017.
42. Varela, M.; Sanchez, M. RMS delay and coherence bandwidth measurements in indoor radio channels in the UHF band. *IEEE Trans. Veh. Technol.* **2001**, *50*, 515–525. [CrossRef]
43. Sayed, A.H. *Adaptive Filters*; John Wiley & Sons: New York, NY, USA, 2011.